materials

MDPI

Article

Heat Transport Architecture Governs the Performance of Large-Area Flexible Thermoelectric Cooling

Jun Pei [1,*,†], Jiazhang Li [2,†], Hao Rao [3], Chun-Yu Li [1], Xianxin Zhang [1], Dai-Bing Zhang [4], Wei Gao [1] and Hezhang Li [5,*]

[1] The Beijing Municipal Key Laboratory of New Energy Materials and Technologies, School of Materials Science and Engineering, University of Science and Technology Beijing, Beijing 100083, China
[2] School of Science, Beijing University of Posts and Telecommunications, Beijing 100876, China
[3] China Satellite Network Application Co., Ltd., Beijing 100160, China
[4] Inner Mongolia Key Lab Nanoscience & Nanotechnology, School of Physical Science and Technology, Inner Mongolia University, Hohhot 010021, China
[5] Department of Precision Instrument, Tsinghua University, Beijing 100084, China
* Correspondence: junpei@ustb.edu.cn (J.P.); lihezhang1202@mail.tsinghua.edu.cn (H.L.)
† These authors contributed equally to this work.

Abstract

Large-area flexible thermal management is increasingly needed for adaptive surface temperature control, wearable electronics and intelligent thermal regulation. Thermoelectric (TE) cooling—solid state, no moving parts, long-lived and fast—is a main route to such systems. Yet as TE cooling scales from localized modules to meter-scale surfaces, the performance limit shifts from the modules to the system-level heat transport architecture, a shift still poorly understood. Using a 2 m × 3 m blanket as benchmark, we build a unified multiphysics framework coupling finite-element simulation with measured dynamic response, and apply it to three architectures: water, air and membrane cooling. We quantify under identical conditions the four mechanisms governing the observed trade-offs: the transport medium sets achievable heat exchange capability; lateral spreading sets surface temperature uniformity; whole-blanket thermal inertia sets dynamic response; and architecture-specific bottlenecks set scalability. Water-cooled blankets serve high-heat-flux scenarios (peak 4.18 kW) but respond slowest (~15 min); air-cooled blankets trade low weight and simple maintenance against moderate capability (1.63 kW, ~5 min); membrane-cooled blankets combine a ~30 s response with an ultrathin build, making them preferable for adaptive surface control. The work reframes large-area TE thermal management as a problem of designing the heat transport architecture rather than of comparing isolated cooling technologies.

Keywords: thermoelectric cooling; surface temperature regulation; flexible thermal management; membrane-cooled system; large-area lateral heat spreading

Check for updates

Academic Editor: Andres Sotelo

Received: 31 October 2026
Revised: 17 November 2026
Accepted: 21 November 2026
Published: 25 November 2026

Copyright: © 2026 by the authors. Licensee MDPI, Basel, Switzerland. This article is an open access article distributed under the terms and conditions of the Creative Commons Attribution (CC BY) license.

1. Introduction

Large-area flexible thermal management is becoming increasingly important for adaptive surface temperature control, intelligent buildings, wearable electronics and other emerging technologies that require dynamic regulation of surface temperature over meter-scale areas [1–4]. Unlike conventional cooling technologies developed for localized heat sources, these applications need active temperature control over meter-scale flexible surfaces while meeting strict limits on weight, structural flexibility, response speed and energy efficiency. Passive approaches—thermal insulation, radiative coatings and phase-change materials—can reduce heat exchange with the environment but cannot respond dynamically to varying

ambient conditions or changing thermal loads [5–7]. Actively controllable thermal management is therefore becoming essential for next-generation intelligent thermal systems.

Among active thermal management technologies, thermoelectric (TE) cooling is attractive because it operates in the solid state [8,9], is compact, controls temperature precisely, pumps heat in both directions and contains no moving mechanical parts [10–13]. Through the Peltier effect, TE modules allow fast and reversible temperature modulation simply by adjusting the applied current, which suits distributed surface temperature regulation [14–16]. Recent progress in high-performance TE materials and flexible device integration has further stimulated work on TE cooling for electronic thermal management, wearable systems, adaptive surface temperature control and intelligent thermal control [17–20]. Hou et al. [21] demonstrated a TE-based active thermal concealment cloak that responds within 2.03 s and controls temperature at the pixel level over centimeter scales.

Extending TE cooling from localized devices to meter-scale flexible surfaces nonetheless raises a fundamentally different engineering problem. In conventional TE cooling, device performance is set mainly by the TE properties of the material together with the interfacial and thermal resistances of the device—the figure of merit (ZT), the cooling power and the coefficient of performance (COP). Once the regulated area grows from the millimeter–centimeter scale to the meter scale, however, cost, system complexity and power consumption all enter, and the limiting factor moves from the TE modules to the system-level heat transport architecture. Efficient heat transport between distributed TE modules and the environment then governs temperature uniformity, heat exchange capacity, dynamic response, structural compactness and, ultimately, the scalability of the whole system. This limited material—limited to architecture—transition is the focus of the present work. Compared with the prior studies, which each address one mechanism or one architecture, the present contribution is the systematic side-by-side comparison of three heat-transport architectures within one unified framework, in which the same four metrics (heat exchange capability, uniformity, response time and scalability) are evaluated and traced to distinct physical mechanisms [9,22,23]. Several engineering strategies [15,24] have been proposed for the large-area heat-management field. However, passive cooling based on highly thermally conductive films [25–27], e.g., graphene or pyrolytic graphite, remains the dominant approach. How to use TE devices to achieve large-area flexible thermal management therefore remains an open problem.

This work builds a unified multiphysics framework to examine three representative TE cooling architectures—water-cooled, air-cooled and membrane-cooled—for large-area flexible thermal management, with a 2 m × 3 m blanket as the baseline. Coupled finite-element simulations and experimental characterization are used to quantify their thermal behavior under one set of benchmark conditions. Rather than assessing single cooling technologies in isolation, the work sets a common benchmark and quantifies the physical mechanisms behind the differences in heat transport capability, temperature uniformity, response dynamics, structural compactness and system scalability. From these analyses we derive a set of engineering design principles for choosing a TE cooling architecture in large-area thermal management, and thereby provide a system-level design framework for scaling TE thermal management from localized devices to meter-scale flexible systems.

2. Materials and Methods

2.1. Simulation Details

The thermal–electrical behavior of the TE cooling systems was simulated in COMSOL Multiphysics (version 6.3) [28,29]. For the water-cooled and air-cooled configurations, the Heat Transfer in Fluids module described convective heat transport in the cooling channels

and was coupled with the Heat Transfer in Solids module for the flexible substrate and the outer film layers. The governing equations for fluid flow and heat transfer are:

$$\text{Continuity equation}: \ \nabla \cdot (\rho u) = 0$$

Navier–Stokes equation (turbulence model):

$$\rho(u \cdot \nabla)u = -\nabla P + \nabla \cdot [(\mu + \mu_t)(\nabla u + (\nabla u)^T)]$$

$$\text{Energy equation for fluid}: \ \rho c_p(u \cdot \nabla T) = \nabla \cdot [(\kappa_f + \kappa_t)\nabla T]$$

where ρ is the fluid density, u is the velocity vector, P is the pressure, μ is the dynamic viscosity, μ_t is the turbulence viscosity, C_p is the specific heat capacity, κ_f is the fluid thermal conductivity and κ_t is the turbulence thermal conductivity.

For the membrane-cooled configuration, the Thermoelectric Effect Multiphysics interface was used, coupling the Heat Transfer in Solids module with the Electric Currents module. The coupled thermal-electrical governing equations are:

$$\text{Heat flux equation}: \ q = -k\nabla T + STJ \text{ and } \nabla \cdot (-k\nabla T + STJ) = J \cdot (-\nabla V)$$

$$\text{Electrical current equation}: \ J = -\sigma(\nabla V + S\nabla T) \text{ and } \nabla J = 0$$

where κ is the thermal conductivity, σ is the electrical conductivity, S is the Seebeck coefficient and V is the electric potential, J is the current density, q is the heat flux density. J includes the Ohmic current term $(\sigma\nabla V)$ and Seebeck coefficient term $(\sigma S\nabla T)$. q includes the conduction heat term $(k\nabla T)$ and the Peltier heat term (STJ). Because S is temperature dependent, both the heat-flux and electrical-current equations include a Thomson term. Peltier heat enters through the thermoelectric energy flux and the heat-flux continuity at the TE interfaces, rather than as an imposed boundary source.

Boundary conditions: the ambient temperature was 300 K for all configurations. For the water-cooled and air-cooled architectures, the inlet fluid temperature was fixed at 288 K with a velocity inlet, and the outlet was set to zero-pressure outflow. Natural and forced convection on the external surfaces were described by convective heat flux boundaries, and the thermal contact between the channels and the blanket layers is not included. For the membrane-cooled architecture, the cold-side temperature of the TE module was controlled by adjusting the applied direct current (DC), with the hot side connected to an ideal heat sink at 300 K, the cold-side temperature being solved self-consistently; by contrast, the 288 K in the water- and air-cooled cases is a prescribed fluid inlet temperature, not a TE cold-side temperature.

Material parameters: the TE modules (commercial TEC1-12706) were modeled with a temperature-dependent Seebeck coefficient ($S \approx 200$ $\mu V \cdot K^{-1}$), electrical conductivity ($\sigma \approx 1 \times 10^5$ $S \cdot m^{-1}$) and thermal conductivity ($\kappa_s \approx 1.5$ $W \cdot m^{-1} \cdot K^{-1}$); the detailed properties of the n-type and p-type materials are given in Figures S1–S3. Water: $\rho = 998$ $kg \cdot m^{-3}$, $C_p = 4182$ $J \cdot kg^{-1} \cdot K^{-1}$, $\kappa_f = 0.6$ $W \cdot m^{-1} \cdot K^{-1}$, $\mu = 1.0 \times 10^{-3}$ Pa·s. Air: $\rho = 1.3$ $kg \cdot m^{-3}$, $C_p = 1005$ $J \cdot kg^{-1} \cdot K^{-1}$, $\kappa_f = 0.026$ $W \cdot m^{-1} \cdot K^{-1}$, $\mu = 1.8 \times 10^{-5}$ Pa·s. The flexible substrate was modeled as nylon film ($\kappa = 0.26$ $W \cdot m^{-1} \cdot K^{-1}$, 0.1 mm thick) and the aluminum coating as $\kappa_s = 200$ $W \cdot m^{-1} \cdot K^{-1}$, 0.1 mm thick. The thermal conductivity of the graphene membrane was treated as a variable parameter, with the other thermophysical properties of graphene kept unchanged, to explore how much conductivity is required.

Mesh and solver settings: owing to the large dimensions (2 m × 3 m), a physics-controlled mesh with an extremely coarse element size was used. The geometry and the corresponding mesh are shown in Figures S4–S10. Stationary and time-dependent solvers were used as appropriate, with a relative convergence tolerance of 10^{-4}. Scaling results for the TE device are given in Figures S11 and S12.

2.2. Experimental Fabrication and Characterization

Water-cooled system: a 2 m × 3 m flexible water-cooled blanket was fabricated from silicone tubes (10 mm outer diameter, 8 mm inner diameter) arranged in a parallel manifold configuration. Fifteen TEC1-12706 modules were integrated into a water-cooled heat exchanger as the cold source. A ten-port barbed manifold distributes chilled water evenly across the tube network. The ten-port manifold describes the experimental assembly, while the numerical model simplifies the tube network as an equivalent channel with tunable radius. Therefore, the experimental hardware and numerical model are described at different levels and do not follow strict one-to-one geometric correspondence. The cold source was maintained by circulating water through the TE-cooled heat exchanger, and an aluminum film (0.1 mm thick, $\kappa \approx 200$ W·m^{-1}·K^{-1}) was laminated onto the outer surface to enhance lateral heat spreading.

Air-cooled system: an air-cooled blanket of the same size (2 m × 3 m) was built from multi-layer co-extruded polyethylene (PE) film (0.2 mm thick) heat-sealed into serpentine channels. The regulated blanket has a projected surface area of 6 m^2. The serpentine channel embedded inside the blanket has a hydraulic diameter of 250 mm. Ambient air was drawn through the channels by a low-pressure fan, and the cold source was provided by fifteen TEC1-12706 modules integrated into an insulated foam-box heat exchanger.

Membrane-cooled system: a compact membrane-cooled unit (20 cm × 20 cm) was assembled from six TEC1-04904 modules (20 mm × 20 mm each) bonded to a graphene thermal diffusion membrane (about 0.1 mm thick, in-plane thermal conductivity about 300 W·m^{-1}·K^{-1} as specified by the supplier). Because membrane cooling relies on solid-state lateral conduction without fluid circulation, the local heat-transport equations are size-independent, but the resulting temperature field depends on the membrane conductivity, thickness, module spacing and distributed load; a compact 20 cm × 20 cm unit is therefore used to demonstrate the mechanism, while the meter-scale extension is treated as a model-based projection. Extending the design to the meter scale adds modules and electrical interconnections rather than changing the heat-transport behavior. The modules were connected in series and driven by a programmable DC supply, and a control algorithm adjusted the current (0–3 A) to hold the target surface temperature.

Temperature measurement: K-type thermocouples (accuracy ±0.5 K) were placed at the inlet and outlet ports and at several positions on the blanket surface. An infrared camera (noise-equivalent temperature difference, NETD, <2 K, rather than absolute accuracy; spatial resolution 32 × 24 pixels) recorded the surface temperature distribution for assessing thermal uniformity.

Performance metrics: four metrics were quantified for the comparison. Heat exchange power (Q_{ex}) is the total heat removed from the surface, calculated from the enthalpy change in the fluid. For the fluid-cooled configurations, it is obtained from $Q_{ex} = \dot{m} \cdot C_p \cdot (T_{out} - T_{in})$, where $\dot{m}$ is the coolant mass flow rate, C_p the specific heat and T_{in}/T_{out} the inlet and outlet temperatures, so that the reported values can be re-verified from the mass flow rate and the measured temperature rise. For comparability across the three architectures, the net heat extracted from the regulated surface is taken as the single primary quantity, and the heat flux density $q = Q_{ex}/A$ (W/m^2) is reported so the architectures can be compared per unit area. Response time (τ) is the time for the surface temperature to reach 95% of its steady-state value after a step change in cooling power. We also distinguish the fluid-side heat pickup (Q_{ex}, the heat carried by the coolant), the surface heat extraction (the heat removed from the regulated surface), the TE cold-side cooling power (Q_c), the TE electrical input (P_{elec}), and the hot-side heat rejection (Q_h), related by $Q_h = Q_c + P_{elec}$; the coefficient of performance is defined at the module level ($COP_m = Q_c/P_{elec}$) and at the system level with the auxiliary power included. The coolant flow rate is reported for each fluid configuration,

with the sign convention that heat absorbed by the fluid is positive. The reported Q_{ex} is the surface-to-fluid heat-exchange capability under a prescribed 288 K coolant inlet, not the net TE cooling power.

Heat exchange power and thermal uniformity were obtained from the finite-element simulation, the response time was measured experimentally, and the system mass and volume were estimated from the fabricated prototypes. A recent study by Xie et al. combined steady-state and transient experimental validation with a grid-independence analysis for a water-cooled thermoelectric component [23]; following that standard, the present work reports the transient response as the one experimentally validated quantity and identifies the corresponding steady-state validation and mesh-independence study as the main remaining steps.

3. Results and Discussion

Figure 1 sketches the three architectures examined here: liquid-cooled, air-cooled and membrane-cooled. In a liquid-cooled architecture, the cold liquid produced by the TE modules is distributed over the whole blanket by forced liquid convection. Water cooling and oil cooling are the two subcategories of liquid cooling and perform at a comparable level; because water is the most common coolant, water cooling is taken as the representative liquid-cooled architecture. An air-cooled architecture works in the same way, except that the cold gas produced by the TE modules is distributed over the blanket by forced airflow. Since the density of air is about one thousandth that of water, air cooling markedly reduces system weight and mechanical complexity, but reaching the same effect as liquid cooling generally requires a much larger volume. A membrane-cooled architecture has no fluid circulation at all and relies on a highly thermally conductive membrane to spread heat laterally by solid-state conduction. The three architectures therefore represent liquid convection, gas convection and lateral solid-state conduction. The following sections analyze how the three architectures differ in the performance metrics of the blanket, trace the physical origin of these differences, and build a system-level framework for understanding and designing TE cooling architectures for large-area flexible thermal management.

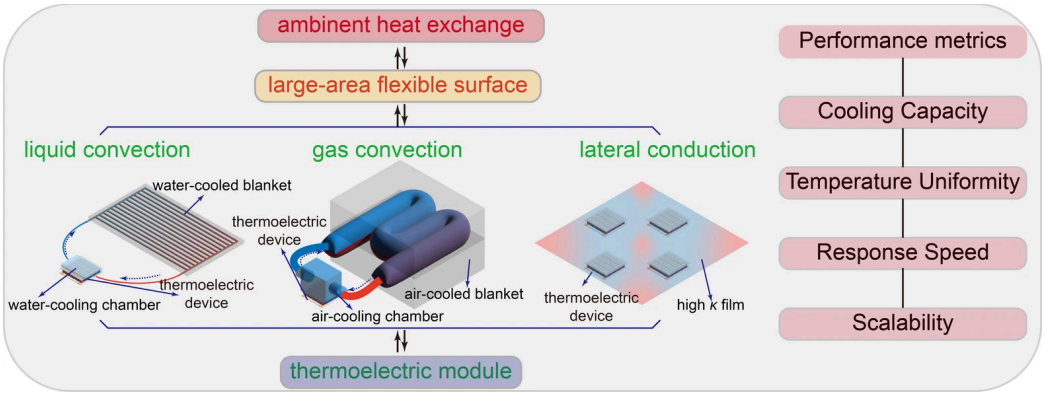

Figure 1. Schematic of the three representative thermoelectric cooling architectures.

3.1. Heat Transport Medium Governs the Achievable Heat Exchange Capability

The first metric for large-area TE thermal management is the heat exchange power: the larger it is, the better the system resists changes in the external environment; the smaller it is, the weaker that resistance. Heat exchange power depends on the cooling power of the TE devices and is also closely tied to the architecture of the blanket. For a fair comparison, the TE modules in both the water-cooled and the air-cooled blankets are assumed to operate

at full power, so that only the heat exchange power of the two blankets under different ambient conditions is examined.

Figure 2 compares the temperature difference (ΔT) and the surface heat exchange power (Q_{ex}) of the three architectures, together with the factors that govern them. Figure 2a shows how the inlet–outlet temperature difference and Q_{ex} of the water-cooled blanket vary with water flow velocity for different tube radii, at an ambient wind speed of 5.5 m/s. As the flow velocity rises, ΔT falls and eventually approaches 0 K, while Q_{ex} first grows almost linearly and then saturates at 4.18 kW. A larger tube radius reaches the same Q_{ex} and ΔT at a lower flow velocity, which also lowers the pressure drop. For a tube radius of 5 mm, a flow velocity of 8.92 m/s gives ΔT = 2.04 K and Q_{ex} = 3.49 kW; for 50 mm, a velocity of only 0.38 m/s gives ΔT = 0.27 K and Q_{ex} = 3.46 kW. In the following, the tube radius of the water-cooled blanket is fixed at 5 mm when temperature uniformity, response speed and system complexity are compared.

Figure 2b shows the same quantities for the air-cooled blanket at different tube radii, again at an ambient wind speed of 5.5 m/s. As with water cooling, ΔT falls and Qex grows quickly as the airflow velocity increases. A larger tube radius reaches the same ΔT and Qex at a lower in-tube gas velocity. At a radius of 50 mm, a gas velocity of 42.1 m/s gives ΔT = 1.08 K and Qex = 2272 W; at 500 mm, ΔT already approaches 0 K at a velocity of only 1 m/s, where Qex is just 1.0 kW. Compared with the water-cooled blanket, the air-cooled blanket therefore needs far larger channels and higher gas velocities to reach a comparable effect, mainly because the volumetric heat capacity of air (about 1.2 kJ·m^{-3}·K^{-1}) is roughly three orders of magnitude lower than that of water (about 4180 kJ·m^{-3}·K^{-1}).

The membrane-cooled architecture has no convective medium and relies entirely on in-plane spreading within the highly conductive membrane to homogenize the blanket surface (Figure 2c). Unlike the water- and air-cooled cases, the membrane itself has a small heat capacity and no medium stores the cooling delivered by the TE modules. Raising the driving current therefore widens the temperature difference between the module surface and the environment, and Q_{ex} increases accordingly. A higher membrane thermal conductivity also gives a larger Q_{ex}: at 1000 W·m^{-1}·K^{-1} and a driving current of 5.6 A, ΔT reaches 16.6 K and Q_{ex} reaches 4.04 kW. This 4.04 kW figure was obtained at the deliberately assumed conductivity of 1000 W·m^{-1}·K^{-1}, whereas the realized membrane is specified at about 300 W·m^{-1}·K^{-1}; at the realized value the corresponding heat-exchange power is about 2.48 kW. The higher figure should therefore be read as an upper bound for an improved membrane, not as a demonstrated performance. A sensitivity study over the membrane conductivity (from 2 to 1000 W·m^{-1}·K^{-1}) shows that the improvement saturates above 500 W·m^{-1}·K^{-1}, so the trend-based conclusions are preserved. The interfacial thermal resistance between the modules and the membrane and the in-plane/out-of-planeanisotropy of the membrane are not characterized, and this is stated as a limitation.

Taken together, the three architectures show how the heat transport medium sets the heat exchange capability: the water-cooled architecture transports heat best because of its large volumetric heat capacity, with a peak heat exchange power of 4.18 kW; the air-cooled architecture drops sharply because of the small volumetric heat capacity of air, with a peak of 2.3 kW; the membrane-cooled architecture has no convective medium, and its peak power depends strongly on the in-plane thermal conductivity of the membrane. These differences persist although all three configurations use the same TE modules, which shows that large-area thermal management differs markedly from centimeter-scale thermal management in scale effects.

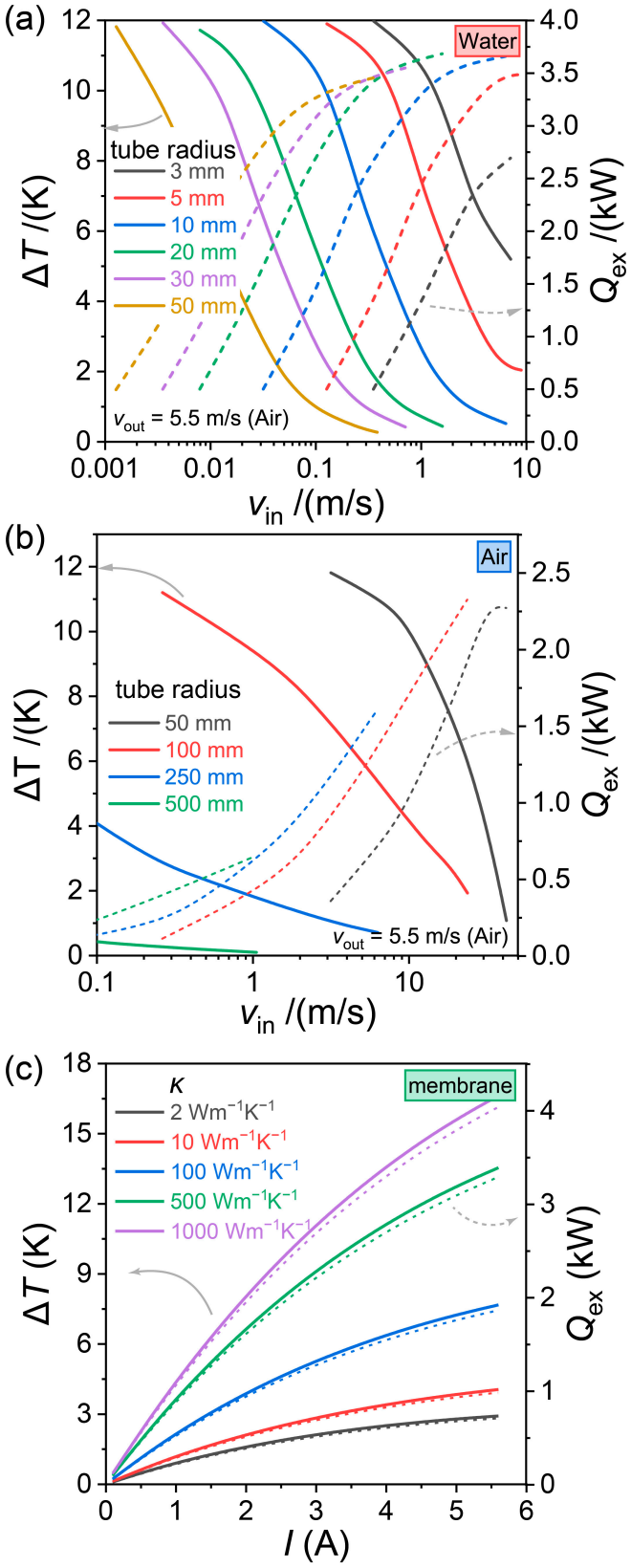

Figure 2. Temperature difference (ΔT) and surface heat exchange power (Q_{ex}) of the three thermoelectric cooling architectures: (**a**) water-cooled; (**b**) air-cooled; (**c**) membrane-cooled. For the water- and air-cooled architectures, ΔT is the temperature difference between the inlet and outlet of the coolant; for the membrane-cooled architecture, ΔT is the difference between the mean surface temperature and the ambient temperature. Solid lines represent ΔT (solid left-pointing arrow), while dashed lines represent Q_{ex} (dashed right-pointing arrow).

3.2. Lateral Heat Spreading Determines Surface Temperature Uniformity

Heat exchange capability alone does not ensure effective large-area thermal management. Heat extracted by distributed TE modules must be redistributed across the regulated surface, otherwise local overcooling and remote hot regions appear. Surface temperature uniformity is therefore set not by the TE cooling power but by the efficiency of lateral heat spreading, and this requirement separates large-area TE thermal management from conventional localized cooling, where the aim is to maximize heat removal at a single spot. On a meter-scale flexible surface, insufficient lateral heat transport inevitably leaves cold patches around individual TE modules and keeps remote regions undercooled. Surface temperature uniformity thus becomes a system-level metric that is largely independent of the intrinsic heat exchange capability of the modules.

Figure 3 shows the factors that govern the surface temperature uniformity of the water-, air- and membrane-cooled configurations. Figure 3a shows that the water-cooled blanket rarely develops local hot spots: at ambient wind speeds of 5 m/s and 20 m/s the surface temperature stays uniform. At 20 m/s, however, the surface temperature of the water-cooled blanket rises even when the internal water velocity reaches 152.79 m/s. When the ambient wind is strong enough, a fast internal water flow can no longer keep the blanket surface cold (Figure S13). The value of 152.79 m/s is a theoretical upper limit from the simulation, which neglects frictional heating of the fluid; in practice the situation would be worse. After an aluminum film is coated on the outer surface, the water-cooled blanket not only stays uniform but also runs clearly cooler than the blanket without the film, even at an internal velocity of only 0.57 m/s. Figure 3b shows the air-cooled blanket at an ambient wind speed of 5 m/s and an internal airflow velocity of 4.24 m/s, where distinct hot spots appear; at 20 m/s and an internal airflow of 20.37 m/s the nonuniformity becomes much stronger. Even with an air-channel radius of 250 mm the temperature uniformity of the air-cooled blanket is clearly worse (Figure S14), because the large channel radius leaves wider gaps between channels and thus places higher demands on the thermal conductivity of the blanket substrate. Coating the air-cooled blanket with a 0.2 mm aluminum film improves its uniformity markedly, yet the surface temperature remains high because of the low volumetric heat capacity of air. For the membrane-cooled blanket, uniformity depends on the driving current of the TE modules and on the thermal conductivity of the membrane. With a deliberately low membrane thermal conductivity of 2 $W \cdot m^{-1} \cdot K^{-1}$, increasing the current lowers the device surface temperature further but makes the surface of the whole blanket less uniform (Figure S15). The heat exchange capability alone does not ensure uniform temperature regulation unless it is matched by sufficient lateral heat transport. When the membrane thermal conductivity is set to 1000 $W \cdot m^{-1} \cdot K^{-1}$, the uniformity improves appreciably even at an ambient wind speed of 20 m/s. The surface temperature uniformity of a thermal management blanket is thus set by lateral heat spreading across the blanket: water- and air-cooled blankets can use the mobility of a fluid medium to speed up lateral spreading, whereas membrane-cooled blankets generally need a membrane of higher thermal conductivity.

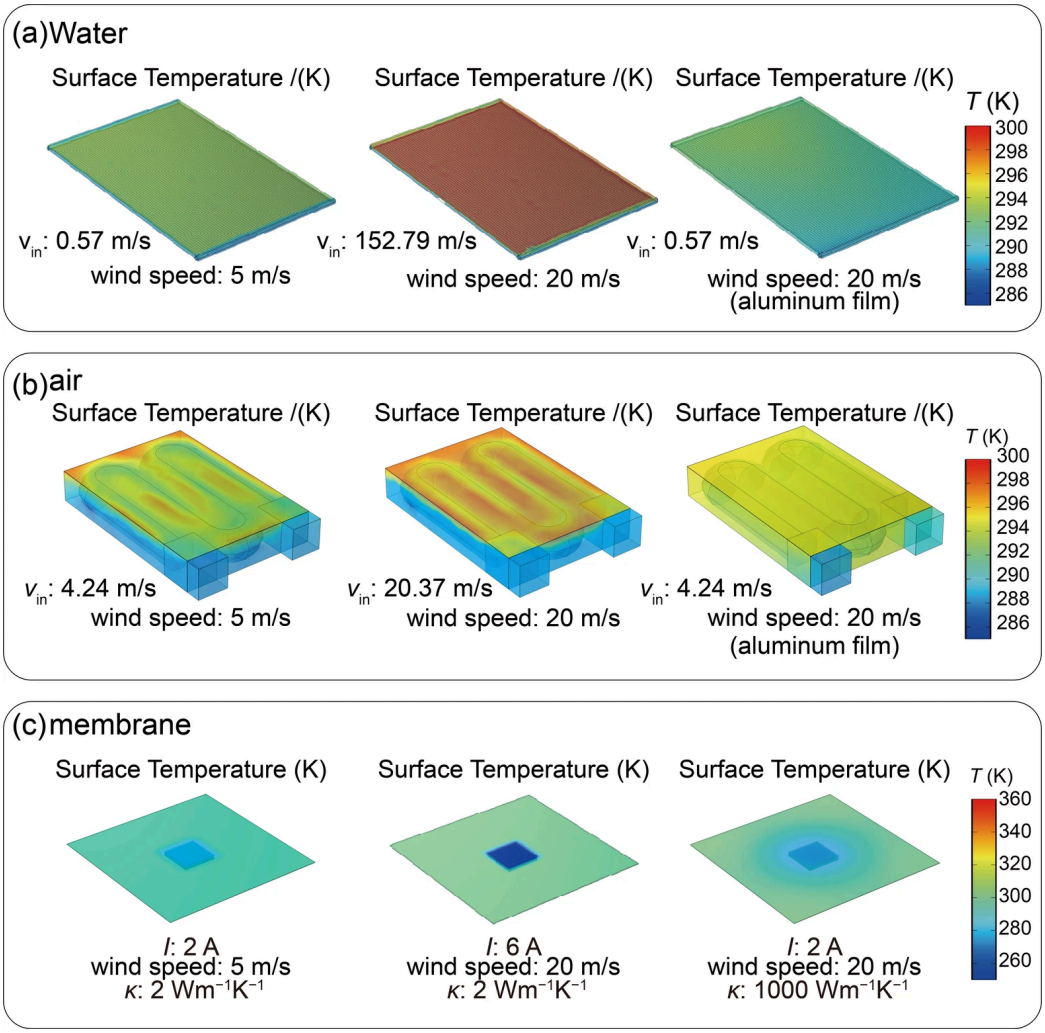

Figure 3. Key factor governing temperature uniformity across the three thermoelectric cooling architectures: (**a**) water-cooled; (**b**) air-cooled; (**c**) membrane-cooled.

3.3. Thermal Inertia Controls Dynamic Response

High heat exchange capability alone is not enough for applications that need adaptive thermal regulation. Large-area TE systems must also respond quickly to continuously varying ambient conditions, which makes the dynamic response a key system-level metric alongside heat exchange capability and temperature uniformity. Figure 4 compares the measured response times of the three blankets: 15 min for water cooling, 5 min for air cooling and 30 s for membrane cooling. The response speed depends on the cooling power of the TE modules and also on the thermal inertia of the blanket itself [30]. The roughly thirty-fold spread shows that transient performance cannot be inferred from steady-state cooling capability. For the water-cooled architecture, the thermal inertia comes mainly from the large heat capacity of the circulating coolant and from the thermal mass of the blanket and its plumbing. Before the regulated surface can reach the target temperature, the entire liquid loop must be cooled, which effectively introduces a large distributed thermal reservoir. That reservoir gives good stability in steady operation, but it also delays the establishment of a new thermal equilibrium after the operating conditions change. Water cooling therefore combines the highest heat removal capability with the slowest dynamic response of the three architectures. Replacing liquid convection with gas convection shrinks the distributed reservoir and shortens the response. The air-cooled system cuts thermal inertia by replacing liquid circulation with forced airflow: with a much lower density and

heat capacity, air stores far less thermal energy, so the surface temperature adjusts faster to a change in electrical input or in the environment. The response still takes minutes, because the large air channels, the flexible substrate and the surrounding structures retain appreciable thermal mass. Continuous exchange with the ambient air adds further disturbance, so the transient response is more sensitive to variations in external convection. The membrane-cooled architecture is the limiting case of minimum thermal inertia. With no fluid circulation at all, heat extracted by the TE modules is carried away by solid-state lateral conduction within the high-thermal-conductivity membrane. Apart from the membrane and the modules themselves, the system holds almost no distributed thermal reservoir, so much less thermal energy is needed to reach a new equilibrium and the surface temperature follows a change in electrical input almost immediately. The measured response time of about 30 s therefore reflects the removal of distributed reservoirs rather than any gain in TE cooling performance.

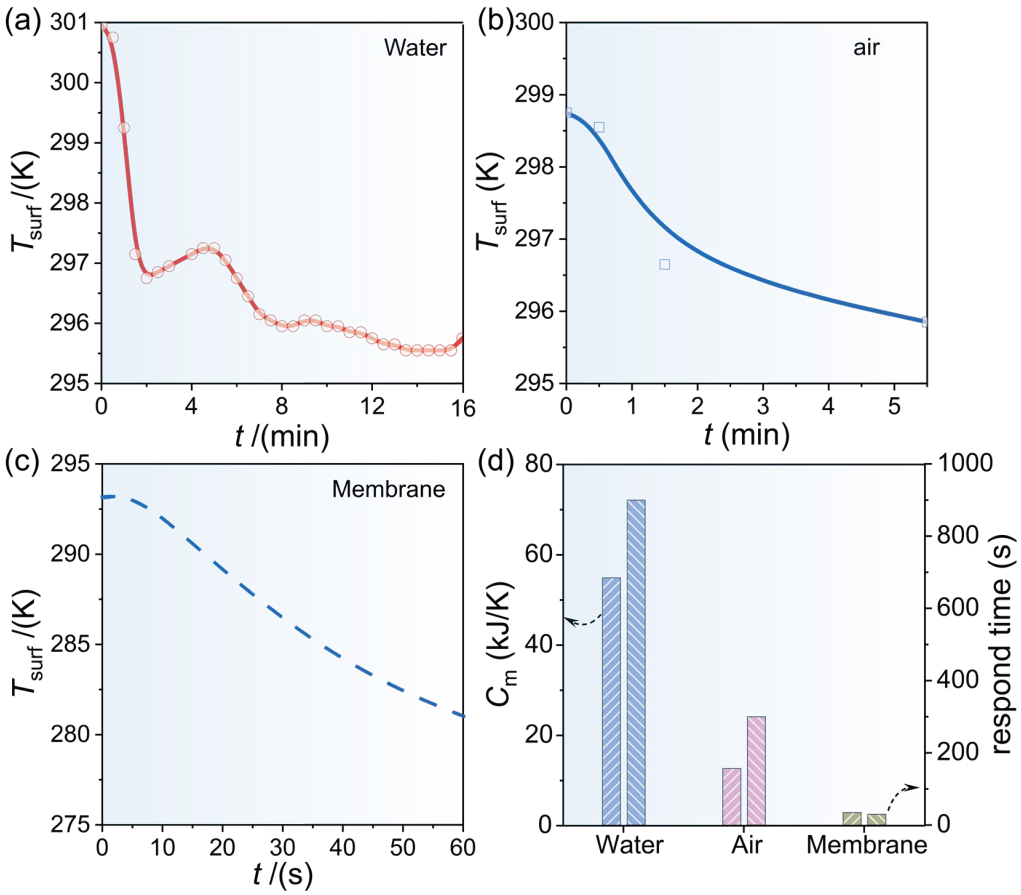

Figure 4. Comparison of the measured response time of the three thermoelectric cooling architectures: (**a**) water-cooled; (**b**) air-cooled; (**c**) membrane-cooled; (**d**) Comparison of the system mass heat capacity (C_m) and response time, where the left bar for each architecture denotes C_m and the right bar denotes the response time.

The measurements were started from a common ambient baseline and driven by a step change in cooling power, with the 95% criterion applied uniformly to each curve in Figure 4. The response-time differences arise from thermal capacitance, thermal resistance and the distributed thermal pathways together, with inertia dominant but not exclusive. The thermal-capacitance values plotted in Figure 4d were estimated from the measured mass and the handbook specific heats of the fluid, substrate and modules, with the contribution of the auxiliary components neglected. These results point to an engineering trade-off between

steady-state performance and transient response. Thermal inertia acts as a passive thermal buffer: architectures with large inertia buffer heat well and hold temperature steadily under fluctuating loads, but respond slowly, whereas architectures with minimal inertia respond quickly but buffer poorly, which makes them more sensitive to external disturbances and local thermal fluctuations (Figure 5).

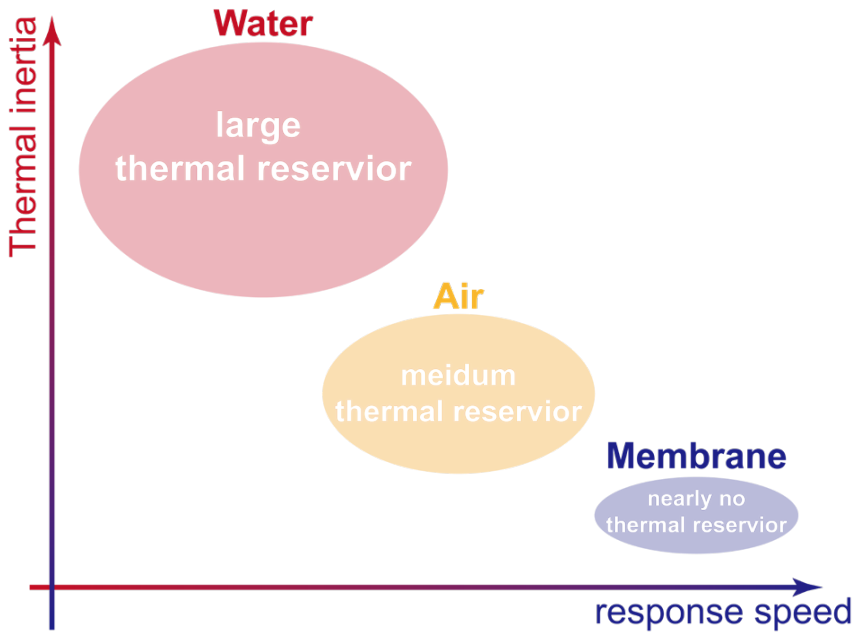

Figure 5. Schematic relationship between response speed and thermal inertia. The bubble area represents the size of the thermal reservoir, which is proportional to the product of mass and specific heat capacity.

3.4. Scalability Is Limited by Architecture-Specific Engineering Bottlenecks

Unlike localized TE cooling devices, large-area flexible thermal management cannot be optimized against a single metric. Practical applications call for simultaneous consideration of heat exchange capability, temperature uniformity, dynamic response, structural weight, occupied volume and implementation complexity. As the three architectures show, a gain in one respect always brings a compromise elsewhere, so the choice of a TE cooling architecture is a multi-objective optimization problem rather than a search for a universally superior solution.

The comparison in Table 1 illustrates these trade-offs. The water-cooled architecture gives the highest Q_{ex}, about 4177.5 W under the present conditions, and occupies a small structural volume thanks to its compact liquid loop. Those advantages come at the cost of a much larger system mass and a long transient response caused by the large thermal reservoir of the circulating coolant. Water cooling is thus effective for concentrated heat removal, but its scalability is limited mainly by the weight of liquid storage, piping and pumping, which grows with the controlled area.

The air-cooled architecture follows a different optimization path. Replacing liquid circulation with airflow cuts system weight and simplifies maintenance by removing pumps and liquid handling. Because the volumetric heat capacity of air is nearly three orders of magnitude lower than that of water, however, much larger flow channels are needed to carry the same thermal energy, so the structural volume grows quickly with cooling demand and eventually becomes the dominant constraint on large-area implementation. The strong dependence on ambient convection also brings uncertainty in outdoor use, where environmental conditions cannot be controlled precisely.

Table 1. Comparison of key performance metrics of the three thermoelectric cooling architectures (water, air, membrane) for large-area flexible thermal management.

Parameter	Water-Cooled	Air-Cooled	Membrane-Cooled
Mass (kg)	23.40	3.28	3.30 (scaled)
Volume (m^3)	0.31	3.30	9.12×10^{-4} (scaled)
Heat exchange power, Q_{ex} (W)	4177.5	1625	2475.6 (scaled)
Heat flux density $q = Q_{ex}/A$ ($W \cdot m^{-2}$)	696.3	270.8	412.6 (projected)
Module operating current I (A)	4.5	4.5	2.0
Module operating voltage V (V)	12	12	4.4
Module temperature difference ΔT (K)	12	12	13
Module cooling capacity Q_c (W)	33	33	5.4
Module electrical input P_{elec} (W)	54	54	8.8
Module-level COP (estimate)	0.61	0.61	0.61
System-level COP (estimate)	0.50	0.43	0.47
Normalized Q_{ex} per electrical input ($W \cdot W^{-1}$)	0.50	0.43	0.47
Response time	~15 min	~5 min	~30 s
Surface temperature at 20 $m \cdot s^{-1}$ wind (K)	291.47 (with Al film)	295.15 (with Al film)	289.06 (with 500 $W \cdot m^{-1} \cdot K^{-1}$)
System complexity	Moderate (pump, plumbing)	Low (fan, ducts)	High (electrical array)
Optimal application	Small, high-heat zones	Large fixed structures	Rapid-response scenarios
Evidence level	Response time measured; Q_{ex} and uniformity simulated; mass/volume estimated	Response time measured; Q_{ex} and uniformity simulated; mass/volume estimated	Response time measured; Q_{ex} and uniformity simulated; mass/volume estimated

The membrane-cooled architecture, by contrast, minimizes both structural volume and thermal inertia by removing fluid circulation altogether. The resulting ultrathin configuration suits flexible thermal management that needs fast temperature modulation with minimal structural intrusion. Its bottleneck moves from thermal transport to electrical integration: scaling membrane cooling from laboratory prototypes to meter-scale surfaces requires many distributed TE modules under coordinated electrical control, and as the system grows, module interconnection, current distribution, power management and reliability become harder than thermal transport itself. The scalability of membrane cooling is thus governed mainly by system integration rather than by cooling performance.

The dominant engineering constraint therefore shifts across the three architectures. For water cooling it is mechanical weight, for air cooling the occupied volume, and for membrane cooling electrical complexity. These bottlenecks arise although all three use identical TE modules, which shows that large-area TE thermal management is constrained by architecture-dependent system characteristics rather than by TE material performance alone.

Energy efficiency is the remaining metric that a heat-exchange comparison alone does not capture. The coefficient of performance is reported in Table 1 at two levels: the module level ($COP_m = Q_c/P_{elec}$) and the system level, which additionally includes the pump, fan

and control-electronics power. Because these auxiliary components were not fitted with power meters, both values are engineering estimates derived from datasheet parameters and stated assumptions rather than measurements. Even at the module level it is clear that TE cooling does not compete with vapor-compression refrigeration on COP; its advantage lies in solid-state, fast, distributed and maintenance-free operation rather than in efficiency. Recent experimental work on water- and air-assisted TE systems has likewise emphasized that COP and electrical power consumption must be reported alongside cooling capability when architectures are compared [31]. A fully instrumented system-level energy audit, including a comparison of the electrical energy required to achieve a specified surface temperature reduction, remains future work.

More broadly, no cooling architecture is optimal for every application. Each occupies a distinct region of the engineering design space. Water-cooled architectures suit applications that need the largest heat exchange capacity within a limited installation volume, such as localized thermal protection or high-power electronics. Air-cooled architectures fit stationary structures where low weight and simple maintenance matter more than compactness, including building-integrated thermal regulation. Membrane-cooled architectures are advantageous for adaptive surface temperature control, wearable thermal regulation and flexible electronic platforms, where fast response, low profile and structural flexibility outweigh the added complexity of electrical integration.

3.5. Engineering Design Framework for TE Cooling Architecture Selection

The mechanisms identified above can be combined into a single engineering framework for choosing a TE cooling architecture to match practical requirements. Large-area TE thermal management is then a multi-objective design problem in which heat exchange capability, temperature uniformity, response speed, structural compactness and system scalability must be balanced at once (Figure 6). Because these metrics stem from different physical mechanisms, no architecture can maximize all of them. The four mechanisms identified here form the basic design dimensions: heat transport capability sets the achievable heat exchange capacity, lateral heat spreading governs surface temperature uniformity, thermal inertia controls the transient response, and architecture-dependent engineering constraints determine scalability. Together they define a design space in which different architectures can be compared quantitatively under the same engineering objectives.

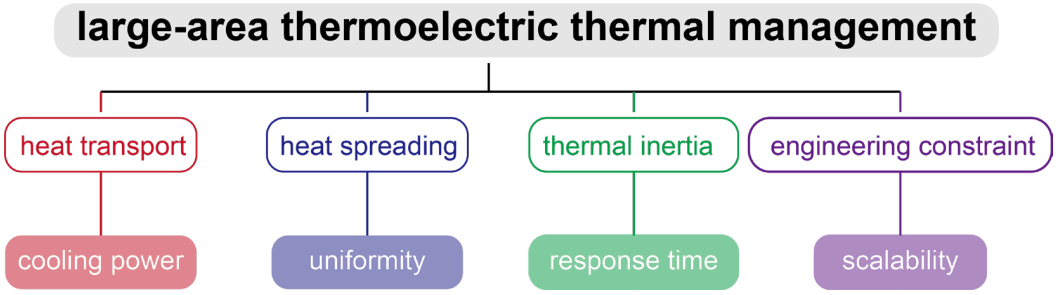

Figure 6. Proposed framework for selecting an architecture for large-area thermoelectric thermal management.

The framework also reveals how design priorities shift as TE systems grow from localized cooling devices to meter-scale thermal management platforms. At small scales, performance is set mainly by the intrinsic characteristics of individual TE modules—cooling power, COP and ZT. As the characteristic dimension grows, the heat transport architecture becomes the dominant factor. Future work on large-area TE thermal management should therefore concentrate on the heat transport network, the distribution of thermal resistance,

structural integration and system architecture, rather than on incremental gains in TE materials alone.

4. Conclusions

In this work, a unified multiphysics framework combining finite-element simulation and an experimental measurement of the dynamic response was built to examine TE cooling architectures for large-area flexible thermal management. Under a common benchmark we quantified four governing principles: (i) the heat transport medium sets the achievable heat exchange capability; (ii) lateral heat spreading determines surface temperature uniformity; (iii) thermal inertia controls the dynamic response; and (iv) scalability is constrained by architecture-specific engineering bottlenecks. No cooling architecture is universally optimal; water-, air- and membrane-cooled architectures meet different requirements. Water-cooled architectures suit applications that need the largest heat exchange capacity within a limited installation volume, such as localized thermal protection or high-power electronics. Air-cooled architectures fit stationary structures where low weight and simple maintenance matter more than compactness, including building-integrated thermal regulation. Membrane-cooled architectures are advantageous for adaptive surface temperature control, wearable thermal regulation and flexible electronic platforms, where fast response, low profile and structural flexibility outweigh the added complexity of electrical integration. As TE thermal management scales from localized devices to meter-scale flexible systems, the dominant design consideration shifts from the TE modules to the heat transport architecture, which provides a system-level framework for future large-area thermal management design. The membrane-cooled architecture was demonstrated only at 20 cm × 20 cm, and its extension to the meter scale still depends on solving the electrical integration problem. Hybrid architectures that combine membrane-based lateral spreading with localized fluid cooling may exploit the complementary strengths of both approaches. Owing to the extremely coarse mesh used for the large dimensions, the reported values should be interpreted as trend-level estimates rather than mesh-converged predictions; a quantitative analysis of the system-level COP and a mesh-independence study are left for future work.

Limitations

Several limitations should be stated explicitly. (i) Because the 2 m × 3 m blankets are discretized with an extremely coarse mesh, no mesh-independence study could be performed and the reported values are trend-level estimates rather than mesh-converged predictions; local refinement of the TE interfaces, the thin membrane layer, the fluid-channel boundaries and the strong-gradient regions was likewise not possible within our computing resources. A validated reduced-order or representative-unit-cell model, as suggested by the reviewer, is identified here as the most promising route to obtain a converged check at acceptable computational cost and will be pursued in future work. (ii) No parametric study of the characteristic length, module spacing, membrane thickness or interfacial thermal resistance was carried out, so the scale dependence of the temperature field is stated qualitatively rather than quantified. (iii) The three architectures use different module types and were operated at different target temperatures; a comparison at matched surface-to-ambient temperature difference, matched heat flux or matched total electrical input, and a comparison of the electrical energy required for a specified temperature reduction could not be completed. (iv) The Reynolds-number estimates place the practical operating range in the laminar or low-turbulence regime, but the turbulence model applied at the extreme velocities was not independently validated. (v) The scaling of total mass, pumping power, channel volume and temperature nonuniformity with regulated area has not been quantified. (vi) The transient measurements started from a common ambient baseline and

the 95% criterion was applied uniformly, but the exact initial offset, excitation amplitude and thermal-capacitance decomposition (fluid, substrate, modules, auxiliaries) were not instrumented, and no RC-model fit was performed. (vii) The temperature uncertainty is limited to the basic instrument specifications (±0.5 K thermocouples, NETD < 2 K infrared); a full uncertainty budget including emissivity correction, sensor positioning and repeat measurements is not available, so error bars are not provided for every comparison. The 32 × 24 pixel infrared images were acquired at a working distance of 10 cm and only cover a local area of roughly 0.04 m^2; this infrared measurement is not used to characterize the temperature uniformity of the full 6 m^2 blanket. (viii) Thermal contact resistance between channels and blanket layers is not included in the current numerical model, and this effect can be considered in follow-up investigations. (ix) A steady-state validation alongside the transient measurement and a grid-independence study are the two steps that would most directly establish quantitative validation. These items define the work needed to turn the present trend-level framework into a validated quantitative design tool.

Supplementary Materials: The following supporting information can be downloaded at https://www.mdpi.com/article/10.3390/ma19234986/s1: Figure S1: Temperature dependence of $|\alpha|$ for both n-type and p-type materials in 12706-type thermoelectric cooler; Figure S2: Temperature dependence of σ for both n-type and p-type materials in 12706-type thermoelectric cooler; Figure S3: Temperature dependence of κ_s for both n-type and p-type materials in 12706-type thermoelectric cooler; Figure S4: Structural model of the water-cooled blanket; Figure S5: Finite element mesh generation for the structural model of the water-cooled blanket; Figure S6: Structural model of the air-cooled blanket; Figure S7: Finite element mesh generation for the structural model of the air-cooled blanket; Figure S8: Structural model of the membrane-cooled blanket; Figure S9: Finite element mesh generation for the structural model of the membrane-cooled blanket; Figure S10: Structural model of the 12706-type thermoelectric cooler; Figure S11: 3D contour plots of surface temperature for the 12706-type thermoelectric device under varying current and wind speed; Figure S12: The current dependence of thermoelectric device performance under different wind speed; Figure S13: 3D contour plots of surface temperature for the water-type blanket under different conditions; Figure S14: 3D contour plots of surface temperature for the air-type blanket under different conditions; Figure S15: 3D contour plots of surface temperature for the membrane-type blanket under different conditions; Figure S16: Infrared image of the thermoelectric module with (a) and without (b) a heat-spreading membrane. Figure S17: Schematic diagram of fluid flow directions for the two blankets. (a) water-cooled blanket; (b) Air-cooled blanket. Table S1. Mesh statistics for the three configurations.

Author Contributions: J.P.: Software, Methodology, Writing—original draft, Supervision. J.L.: Writing—original draft, Investigation, Conceptualization. H.R.: Investigation, Data curation. C.-Y.L.: Investigation. X.Z.: Software, Investigation. D.-B.Z.: Software, Investigation. W.G.: Software, Methodology, Investigation. H.L.: Writing—review and editing, Validation, Resources, Conceptualization. All authors have read and agreed to the published version of the manuscript.

Funding: This work was financially supported by the National Natural Science Foundation of China (Nos. 52302211 and 52401285), the State Key Laboratory of New Ceramic and Fine Processing Tsinghua University (No. KFZD202303), the Guangdong Basic and Applied Basic Research Foundation (No. 2022A1515111100), and the Fundamental Research Funds for the Central Universities (No. FRFTP-24-005A).

Data Availability Statement: The original contributions presented in this study are included in the article/Supplementary Materials. Further inquiries can be directed to the corresponding authors.

Conflicts of Interest: Author Hao Rao was employed by the company China Satellite Network Application Co., Ltd. The remaining authors declare that the research was conducted in the absence of any commercial or financial relationships that could be construed as a potential conflict of interest.

Abbreviations

The following abbreviations are used in this manuscript:

TE	thermoelectric
ZT	Thermoelectric figure of merit
COP	Coefficient of performance
PE	Polyethylene

References

1. Liu, Q.; Tian, B.; Liang, J.; Wu, W. Recent Advances in Printed Flexible Heaters for Portable and Wearable Thermal Management. *Mater. Horiz.* **2021**, *8*, 1634–1656. [CrossRef] [PubMed]
2. Su, Y.; Ma, C.; Chen, J.; Wu, H.; Luo, W.; Peng, Y.; Luo, Z.; Li, L.; Tan, Y.; Omisore, O.M.; et al. Printable, Highly Sensitive Flexible Temperature Sensors for Human Body Temperature Monitoring: A Review. *Nanoscale Res. Lett.* **2020**, *15*, 200. [CrossRef] [PubMed]
3. Zhou, P.; Jiang, G.; Wang, Y.; Tian, Y.; Zhang, X. Self-Adaptive and Large-Area Sprayable Thermal Management Coatings for Energy Saving. *Nat. Commun.* **2025**, *16*, 3791. [CrossRef] [PubMed]
4. Huang, J.; Yuan, L.; Liao, J.; Wang, Y.; Liu, Y.; Ji, C.; Huang, C.; Luo, X. Dynamic Infrared Radiation Regulator Enabling Positive and Reversible Modulation of Emissivity and Temperature. *Adv. Mater. Technol.* **2024**, *9*, 2400522. [CrossRef]
5. Hu, Y.; Zhang, Z.; Zhang, D.; Xiu, F.; Zhang, M.; Dong, X.; Song, C.; Zhang, Z.; Chen, C.; Xie, X.; et al. Adaptive and Remote Thermoregulation Enabled with a Highly Stable Transparent Flexible Heating Film. *ACS Appl. Energy Mater.* **2022**, *5*, 8892–8899. [CrossRef]
6. Wang, Z.; Ju, Q.; Zhang, X.; Sun, S.; Chen, M.; Zhou, X.; Gu, H.; Zhang, B.; Zhi, H.; Chen, Y.; et al. Large-Area Flexible Thermal Control Films via Balancing Low Solar Absorptivity and Low Infrared Emissivity. *Appl. Surf. Sci.* **2026**, *721*, 165488. [CrossRef]
7. Yu, H.; Lu, J.; Yan, J.; Bai, T.; Niu, Z.; Ye, B.; Cheng, W.; Wang, D.; Huan, S.; Han, G. Selective Emission Fabric for Indoor and Outdoor Passive Radiative Cooling in Personal Thermal Management. *Nano-Micro Lett.* **2025**, *17*, 192. [CrossRef] [PubMed]
8. Pei, J.; Cai, B.; Zhuang, H.-L.; Li, J.-F. Bi2Te3-Based Applied Thermoelectric Materials: Research Advances and New Challenges. *Natl. Sci. Rev.* **2020**, *7*, 1856–1858. [CrossRef] [PubMed]
9. Park, S.J.; Bang, K.M.; Kim, B.; Ziolkowski, P.; Jeong, J.-R.; Jin, H. Adaptive Thermoelectric Cooling System for Energy-Efficient Local and Transient Heat Management. *Appl. Therm. Eng.* **2022**, *216*, 119060. [CrossRef]
10. Li, Z.; Yang, X.; Gao, Z.; Wang, J.; Xue, Y.; Wang, J.; Cao, Q.; Ding, Z.; Wang, S. Remarkable Average Thermoelectric Performance of the Highly Oriented Bi(Te, Se)-Based Thin Films and Devices. *J. Mater.* **2024**, *10*, 366–376. [CrossRef]
11. Gao, Z.; Hou, S.; Liu, X.; Xue, Y.; Li, Z.; Zhao, Q.; Wang, J.; Li, Z.; Wang, S. Post-Selenization Tailored Carrier-Crystallographic Synergy in c-Axis Bi2Se3 Thin Films for Advanced Thermoelectrics. *J. Mater.* **2026**, *12*, 101099. [CrossRef]
12. Zhao, Q.; Fan, Z.; Wang, Y.; Liu, Q.; Dong, X.; Wu, X.; Shan, Z.; Zhu, H.; Li, Z.; Wang, S.; et al. Atomic-Defect-Suppressed Pristine p-Type Bi0.3Sb1.7Te3 as Robust High-Performance Thermoelectrics for Power Generation and Cooling. *J. Mater.* **2025**, *11*, 101090. [CrossRef]
13. Wang, Q.; Song, S.; Yang, X.; Liu, Z.; Ma, Y.; San, X.; Wang, J.; Zhang, D.; Wang, S.-F.; Li, Z. Incorporating Element Doping and Quantum Dot Embedding Effects to Enhance the Thermoelectric Properties of Higher Manganese Silicides. *J. Mater.* **2021**, *7*, 377–387. [CrossRef]
14. Zianni, X. Thermoelectric Metamaterials: Nano-Waveguides for Thermoelectric Energy Conversion and Heat Management at the Nanoscale. *Adv. Electron. Mater.* **2021**, *7*, 2100176. [CrossRef]
15. Sullivan, O.; Gupta, M.P.; Mukhopadhyay, S.; Kumar, S. Array of Thermoelectric Coolers for On-Chip Thermal Management. *J. Electron. Packag.* **2012**, *134*, 021005. [CrossRef]
16. Chauhan, N.S.; Mori, T. Cooler, Stronger, Smaller: Improving Thermoelectric Cooling. *Natl. Sci. Rev.* **2024**, *12*, nwae445. [CrossRef] [PubMed]
17. Liu, Y.; Cheng, H.-Y.; Malen, J.A.; Xiong, F. Thermoelectric Active Cooling for Transient Hot Spots in Microprocessors. *Nat. Commun.* **2024**, *15*, 4275. [CrossRef] [PubMed]
18. Lu, Y.; Fan, X.; Luo, J.; Liu, W.; Zhao, L. Application of Thermoelectric Cooling on Chip Thermal Management. *J. Chin. Ceram. Soc.* **2025**, *53*, 849–861. [CrossRef]
19. Baokun, D.; Ting, Z.; Fan, H. Research Progress and Application of Flexible Thermoelectric Materials. *Prog. Chem.* **2023**, *35*, 433. [CrossRef]
20. Jin, J.; Hou, Y.; Li, C.; Liang, X.; Sun, X.; Ding, Q.; Zhang, X.; Xia, Z.; Yan, S.; Yang, Y.; et al. High-Performance Waterproof Flexible Thermoelectric Generators for Self-Powered Electronics. *Nano Energy* **2024**, *132*, 110388. [CrossRef]
21. Hou, Y.; Liang, X.; Li, Z.; Ding, Q.; Zhu, Z.; Sun, X.; Li, C.; Zhou, W.; Cao, W.; Yu, Y.; et al. Thermoelectric Device for Active Thermal Concealment, Deception and Messaging. *Nat. Commun.* **2025**, *16*, 9888. [CrossRef] [PubMed]

22. Lim, H.; Kang, Y.-K.; Jeong, J.-W. Thermoelectric Radiant Cooling Panel Design: Numerical Simulation and Experimental Validation. *Appl. Therm. Eng.* **2018**, *144*, 248–261. [CrossRef]
23. Xie, X.; Zhang, X.; Zhang, J.; Qiao, Q.; Jia, Z.; Wu, Y.; Song, X.; Zhao, H.; Li, Q. Performance Analysis and Optimal Design of a Water-Cooled Thermoelectric Component for Air Cooling Based on Simulation and Experiments. *Int. Commun. Heat Mass Transf.* **2023**, *141*, 106576. [CrossRef]
24. Wang, C.-C.; Hung, C.-I.; Chen, W.-H. Design of Heat Sink for Improving the Performance of Thermoelectric Generator Using Two-Stage Optimization. *Energy* **2012**, *39*, 236–245. [CrossRef]
25. Lu, J.; Ming, X.; Cao, M.; Liu, Y.; Wang, B.; Shi, H.; Hao, Y.; Zhang, P.; Li, K.; Wang, L.; et al. Scalable Compliant Graphene Fiber-Based Thermal Interface Material with Metal-Level Thermal Conductivity via Dual-Field Synergistic Alignment Engineering. *ACS Nano* **2024**, *18*, 18560–18571. [CrossRef] [PubMed]
26. Huang, K.; Pei, S.; Wei, Q.; Zhang, Q.; Guo, J.; Ma, C.; Cheng, H.-M.; Ren, W. Highly Thermally Conductive and Flexible Thermal Interface Materials with Aligned Graphene Lamella Frameworks. *ACS Nano* **2024**, *18*, 23468–23476. [CrossRef] [PubMed]
27. Luo, W.; Wei, B.; Luo, T.; Li, B.; Zhu, G. 3D Network of Liquid Metal-Embedded Graphene via Surface Coating for Flexible Thermal Management. *Small* **2024**, *20*, 2406574. [CrossRef] [PubMed]
28. Hasan, M.K.; Üstüner, M.A.; Mamur, H.; Bhuiyan, M.R.A. Enhancing Bi2Te2.70Se0.30 Thermoelectric Module Performance through COMSOL Simulations. *Thermo* **2024**, *4*, 185–201. [CrossRef]
29. Wu, A.; Zhang, K.; Wang, W.; Pan, R.; Wang, S.; Luo, X.; Chen, H. Multi-Dimensional Simulation of the Segmented Thermoelectric Generator Applied in the Heat Pipe Reactor Based on COMSOL. *Ann. Nucl. Energy* **2024**, *208*, 110750. [CrossRef]
30. Dorji, G.; Minakshi, M.; Ariga, K.; Shrestha, L.K. Binary Transition Metal Oxides vs. Binary Metal Oxides for Electrochemical Supercapacitors: Performance, Challenges, and Future Prospects. *J. Energy Storage* **2026**, *147*, 120116. [CrossRef]
31. Mohamed, E.S. Experimental Evaluation of the Thermoelectric Package Air Conditioning for an Automotive Interior Application. *Int. J. Refrig.* **2025**, *174*, 34–46. [CrossRef]

Disclaimer/Publisher's Note: The statements, opinions and data contained in all publications are solely those of the individual author(s) and contributor(s) and not of MDPI and/or the editor(s). MDPI and/or the editor(s) disclaim responsibility for any injury to people or property resulting from any ideas, methods, instructions or products referred to in the content.